Electrokinetic secondary-flow behavior in a curved microchannel under dissimilar surface conditions

Myung-Suk Chun*

Complex Fluids Research Laboratory, Korea Institute of Science and Technology (KIST), Seongbuk-gu, Seoul 136-791, Republic of Korea

(Received 20 July 2010; revised manuscript received 18 January 2011; published 22 March 2011)

The curved channel appears to be indispensable for the lab-on-chips systems because it provides a convenient scheme for increasing the channel length per unit chip area in the direction of net flow. A secondary Dean flow in curved rectangular microchannels is examined by applying the finite-volume scheme with a semi-implicit method for pressure-linked equations (SIMPLE) algorithm for the pressure-driven electrokinetic transport. This framework is based on the theoretical model coupled with the full Poisson-Boltzmann, Navier-Stokes, and the Nernst-Planck principles of net charge conservation [Yun *et al*., Phys. Fluids **22**, 052004 (2010)]. The effect of a dissimilar wall condition on the secondary flow at the turn is explored by considering different configurations of channel wall having complementary aspect ratios (i.e., ratio of the channel height to the channel width, $H/W =$ 0.25 and 4.0) with combinations of hydrophilic glass and hydrophobic polydimethylsiloxane surfaces. Simulation results exhibit that, contrary to the case of general narrow-bore channels, the streamwise axial velocity tends to shift toward the inner wall caused by a stronger effect of the spanwise pressure gradient, according to a sufficiently low Dean number. The increasing rate of this shift with increasing curvature ratio is more significant in the shallow (or low-aspect-ratio) channel, due to the effect of greater distance traveled by the fluid along the outer wall. The curvature introduces the presence of pairs of counter-rotating vortices perpendicular to the flow direction. Comparing between shallow and deep (or high-aspect-ratio) channels allows us to identify that the patterns of axial velocity and vorticity are altered by the heterogeneity effect of surfaces occupying a large area. The total magnitude of vorticity at the cross section of the channel increases with increasing slip length, due to the contribution of enhanced axial velocity driven by the slip, while there is no fluid-slip dependency for the slip length of less than about 50 nm.

DOI: 10.1103/PhysRevE.83.036312 PACS number(s): 47.57.jd, 47.61.Fg, 83.50.Rp, 47.15.G−

I. INTRODUCTION

In the microchannel, turn geometry becomes an essential tool, especially in single cell or particle manipulations via the trap-and-release mechanism [1]. It also allows chaotic advection generating passive mixing at low Reynolds numbers and the controllable reaction residence for synthetic applications [2,3]. In microfluidic devices implying pressure-driven flows, the improved fractionation efficiency can be attained by folding the straight channel into the shape of a serpentine curved channel [4]. In fluid flows through a curved channel, secondary flow arises due to a mismatch of streamwise velocity between fluid in the channel center and in the near-wall regions. The ability to figure out the role of secondary flow in the axial dispersion and the enhanced mixing performance arising from the channel curvature is pertinent to either the rational design or operation of integral components of lab-on-chips (LOCs) devices.

Microfluidics (and more recently, nanofluidics) involving electrokinetic phenomena has attracted attention because the electric double layer (EDL) makes the transport behavior deviate from that described by the laminar flow equation in general [5–7]. Since the earlier works traced back to the 1960s [8,9], although many studies have contributed to elucidating the electrokinetic flow phenomena, note that those studies were almost confined to an analysis with applying straight channels [10–15]. Chun *et al*. [13,14] developed the explicit model accompanying the numerical scheme for electrokinetic flows in either cylindrical or rectangular microchannels. The model was based on the analysis of the Navier-Stokes (N-S) momentum equation coupled with the nonlinear Poisson-Boltzmann (P-B) field, taking further consideration of the Nernst-Planck (N-P) equation for charge conservation. As a continued study, they have treated recently the problem of electrokinetic flow in a curved rectangular microchannel [16] to recognize the skewed pattern in a streamwise velocity by stressing the geometry effect.

In practical applications, a microchannel frequently may be fabricated with the substrate and covering plate of dissimilar materials and thus possesses different surface properties on each side of the channel wall [17]. The resulting surface heterogeneity due to unequal surface charge and fluid slip at solid surfaces leads to irregular flow patterns, nonuniform species transport, and decrease of the turn-induced band broadening. Nevertheless, explicit analyses have not been attempted, even in the case of the most widely used microchannels of glass-polydimethylsiloxane (PDMS) illustrated in Fig. 1. Furthermore, the surface heterogeneity can be introduced intentionally by chemical modification of the inner surface to induce a vortex or secondary flow.

The charge property of the channel surface is characterized by the electrokinetic zeta potential measurement, although it does not give direct information about the electric surface potential itself. The zeta potential is referred to as the potential at the shear plane, which is an imaginary plane of the mobile inner part of the EDL, and the no-slip flow condition is assumed to apply on this plane [18]. Another key question concerning the boundary condition (BC) at the channel wall

*mschun@kist.re.kr

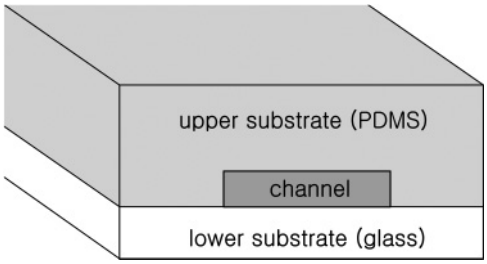

FIG. 1. Schematic of a frontal section of the rectangular microchannel comprised of a hydrophobic polymer and a hydrophilic glass.

is fluid slip, which is a function of the wettability indicated by the contact angle. According to Navier's fluid-slip condition [19], a definition of a general slip length (sometimes, slip coefficient) β at a hydrophobic (solvophobic) rigid boundary, with the unit normal $\boldsymbol{m}$ directed into the fluid, linearly relates the tangential component of velocity $\boldsymbol{v}_t$ at the wall to the wall-shear strain rate [20,21]

$$\boldsymbol{v}_t = \beta\, \boldsymbol{m} \cdot [\nabla \boldsymbol{v} + (\nabla \boldsymbol{v})^T]. \tag{1}$$

Here, β can be regarded as the characteristic length normal to the wall, representing the degree of absence of the shearing force. Since the normal component of velocity $\boldsymbol{v}_n$ $(=\boldsymbol{v} \cdot \boldsymbol{m})$ is governed by conservation of mass, $\boldsymbol{v}_n = 0$ for a stationary and impermeable solid. This is referred to as the no-penetration condition.

In this paper, numerical results of the vorticity change are reported to carefully examine the Dean vortex-based secondary-flow behavior of electrokinetic transport in curved channels with complementary aspect ratios of 0.25 and 4.0. Since improved mixing and precise control over fluid interfaces can be achieved by utilizing the secondary Dean flows, this subject is an important new insight into microfluidics and possibly nanofluidics. This study conducts rectangular channels of uniform width, the dimension of which is on the order of micrometers, which are commonly used in actual microfluidic systems for performing chemical and biological analysis. The semi-implicit method for pressure-linked equations (SIMPLE) algorithm was employed with an alternating-direction-implicit (ADI) method, which is considered as the well-established numerical technique for simulating the pressure-velocity coupling problem [22]. The effect of dissimilar wall conditions was elucidated by addressing different configurations of channel surface with hydrophilic glass and hydrophobic PDMS. Both the skewed pattern of axial velocity and the vorticity profile were reported with variations of the channel geometry, including the fluid-slip contribution.

II. MODEL AND COMPUTATIONAL METHODS

A. Microchannel geometry

We consider a situation for pressure-driven and steady-state electrokinetic flow through a curved rectangular microchannel of the width W and the height (or, referred to as depth) H with a uniform curvature, as presented in Fig. 2. The curvature radius $R_C = dz/d\theta$ is measured from the axis of curvature, and

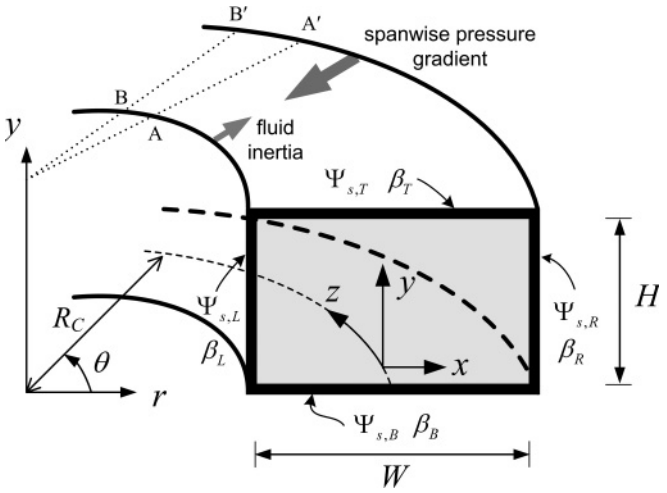

FIG. 2. The curved channel geometry with dissimilar surface properties and coordinates system.

$x(= r - R_C)$ and z are the spanwise and streamwise distance along the channel axis, respectively. Providing the spanwise and longitudinal velocities, the stream function S is defined as $v_r = (1/r)(\partial S/\partial y)$ and $v_y = -(1/r)(\partial S/\partial r)$. By the relations between the rectangular Cartesian coordinates and the global toroidal coordinate system, the vorticity vector $\boldsymbol{\omega}$ $(=\nabla \times \boldsymbol{v})$ yields its θ and z components, given by

$$\omega_\theta = \partial v_y/\partial r - \partial v_r/\partial y, \quad \omega_z = \partial v_y/\partial x - \partial v_x/\partial y. \tag{2}$$

For the local Cartesian coordinates, it is obtained, after some rearrangement of terms, that

$$\frac{\partial^2 S}{\partial x^2} - \frac{1}{x + R_C}\frac{\partial S}{\partial x} + \frac{\partial^2 S}{\partial y^2} = -(x + R_C)\omega_z = \left(\frac{x + R_C}{2R_h}\right)\nabla^2 S, \tag{3}$$

where the hydraulic radius R_h is given as $HW/(H+W)$.

B. The electrokinetic microflow and ion transport

When the nonconductive and charged surface is in contact with an electrolyte in solution, the electrostatic charge would influence the distribution of nearby ions, and the electric field is consequently established [13]. The nonlinear P-B equation governing the electric potential ψ field is given as

$$\nabla^2 \Psi = \kappa^2 \sinh \Psi, \tag{4}$$

where the dimensionless electric potential Ψ denotes $\Lambda e\psi/kT$ and the inverse EDL thickness is defined by $\kappa = \sqrt{2n_b\Lambda_i^2 e^2/\varepsilon kT}$ with the valence of i ions Λ_i. Here, the symmetric $(\Lambda\text{-}\Lambda)$ electrolytes are applied, in which both cations and anions have the same valences. The electrolyte concentration in bulk solution at the electroneutral state n_b $(1/\mathrm{m}^3)$ is equal to a product of Avogadro's number N_A and bulk electrolyte concentration (mM). e is the elementary charge, ε is the dielectric constant given as a product of the dielectric permittivity of a vacuum and the relative permittivity for aqueous fluid (=78.9), and kT is the Boltzmann thermal energy at room temperature (RT).

The Boltzmann distribution of the ionic concentration of type i [i.e., $n_i = n_b \exp(-\Lambda_i e\psi/kT)$] provides a local charge density $\Lambda_i e n_i$. Since the net charge density ρ_e is defined by $\Sigma_i \Lambda_i e n_i [= \Lambda e(n_+ - n_-)]$, one can determine $\rho_e = -2\Lambda e n_b \sinh\Psi$. Equation (4) is coupled with the constant-potential surface BCs imposed on each side of the uniformly charged wall: $\Psi = \Psi_{s,L}$ at $x = -W/2$, $\Psi = \Psi_{s,R}$ at $x = W/2$, $\Psi = \Psi_{s,B}$ at $y = 0$, and $\Psi = \Psi_{s,T}$ at $y = H$. As displayed in Fig. 2, the subscripts T, B, R, and L correspond to top, bottom, right-sided, and left-sided channel wall. For the case of low potential ($|\Psi_s| \leqslant 1$), the linearized P-B equation (i.e., Debye-Hückel ansatz) can be applied instead of the full P-B version.

The velocity field for an incompressible Newtonian aqueous fluid at the steady state obeys the N-S equation

$$\rho(\boldsymbol{v}\cdot\nabla\boldsymbol{v}) = -\nabla p + \mu\nabla^2\boldsymbol{v} + \boldsymbol{F}, \tag{5}$$

where ρ and μ indicate the density and viscosity of the fluid, respectively. Since the details regarding this part were presented in the previous work [16], it needs to be described briefly here. The velocity profile for the straight channel with uncharged wall is described by the Stokes flow ($\mu\nabla^2\boldsymbol{v} = \nabla p$). Since the end effects are negligible ($\partial/\partial\theta = 0$), the laminar flow velocity and the pressure are expressed as $\boldsymbol{v} = [v_r(r,y), v_y(r,y), v_\theta(r,y)]$ and $p = p(r,y,\theta)$, respectively. The body force F per unit volume ubiquitously caused by the θ-directional action of flow-induced electric field E_θ on $\rho_e(r,y)$ can be written as $F_\theta = \rho_e E_\theta$. Neglecting the spanwise dependence of E_θ, it is defined by the flow-induced streaming potential ϕ as $E_\theta(\theta) = -d\phi(\theta)/d\theta$. Each component of the N-S equation is determined with utilization of the Cartesian coordinates given by

$$r \to x: \quad \rho\left(v_x\frac{\partial v_x}{\partial x} + v_y\frac{\partial v_x}{\partial y} - \frac{v_z^2}{r}\right) = -\frac{\partial p}{\partial x} + \mu\left[\frac{1}{r}\frac{\partial}{\partial x}\left(r\frac{\partial v_x}{\partial x}\right) - \frac{v_x}{r^2} + \frac{\partial^2 v_x}{\partial y^2}\right], \tag{6}$$

$$y \to y: \quad \rho\left(v_x\frac{\partial v_y}{\partial x} + v_y\frac{\partial v_y}{\partial y}\right) = -\frac{\partial p}{\partial y} + \mu\left[\frac{\partial^2 v_y}{\partial x^2} + \frac{1}{r}\frac{\partial v_y}{\partial x} + \frac{\partial^2 v_y}{\partial y^2}\right], \tag{7}$$

$$\theta \to z: \quad \rho\left(v_x\frac{\partial v_z}{\partial x} + v_y\frac{\partial v_z}{\partial y} + \frac{v_x v_z}{r}\right) = -\frac{R_C}{r}\left(\frac{\partial p}{\partial z} - \rho_e\frac{\partial\phi}{\partial z}\right) + \mu\left[\frac{1}{r}\frac{\partial}{\partial x}\left(r\frac{\partial v_z}{\partial x}\right) - \frac{v_z}{r^2} + \frac{\partial^2 v_z}{\partial y^2}\right], \tag{8}$$

where the fluid velocity in Eq. (8) is coupled with ϕ .

The slip length β, which is assumed to be a material parameter, is the local equivalent distance below the solid surface at which the no-slip BC ($\beta = 0$) would be satisfied if the flow field were extended linearly outside of the physical domain. Applying Eq. (1) to the wall of the curved channel in Fig. 2 denotes the form

$$v_\theta = \beta\left[\frac{1}{r}\frac{\partial v_r}{\partial\theta} + r\frac{\partial}{\partial r}\left(\frac{v_\theta}{r}\right)\right]. \tag{9}$$

Since the normal velocity v_r vanishes on the surface, we obtain a generalized slip condition at a surface with R_C as

$$v_\theta = \left(\frac{1}{\beta} + \frac{1}{R_C}\right)^{-1}\frac{\partial v_\theta}{\partial r} = \frac{\beta R_C}{(\beta + R_C)}\frac{\partial v_\theta}{\partial r}. \tag{10}$$

Then, the slip length β^C on a curved surface is expressed as $\beta R_C/(\beta + R_C)$. For hydrophobic curved surfaces in Fig. 2, each BC is applied as $v_x|_{y=0} = \beta_B(\partial v_x/\partial y)_{y=0}$, $v_x|_{y=H} = -\beta_T(\partial v_x/\partial y)_{y=H}$, $v_y|_{x=-W/2} = \beta_L(\partial v_y/\partial x)_{x=-W/2}$, $v_y|_{x=W/2} = -\beta_R(\partial v_y/\partial x)_{x=W/2}$, $v_z|_{y=0} = \beta_B(\partial v_z/\partial y)_{y=0}$, $v_z|_{y=H} = -\beta_T(\partial v_z/\partial y)_{y=H}$, $v_z|_{x=-W/2} = \beta_L^C(\partial v_z/\partial x)_{x=-W/2}$, and $v_z|_{x=W/2} = -\beta_R^C(\partial v_z/\partial x)_{x=W/2}$, where $\beta_L^C = \beta_L(R_C - W/2)/[(R_C - W/2) - \beta_L]$ and $\beta_R^C = \beta_R(R_C + W/2)/[(R_C + W/2) - \beta_R]$. The straight channel ($W/R_C \to 0$) takes a change in two conditions, leading to $v_z|_{x=-W/2} = \beta_L(\partial v_z/\partial x)_{x=-W/2}$ and $v_z|_{x=W/2} = -\beta_R(\partial v_z/\partial x)_{x=W/2}$. Since the velocity becomes a maximum at the center of the channel, the sign of the velocity gradient changes into negative along the axis.

Next, the net current conservation ($\nabla\cdot\boldsymbol{I} = 0$) is applied in the microchannel taking into account the N-P equation. The ionic flux in terms of a number concentration ($1/\mathrm{m}^2$ s) is possible to describe by the contribution owing to convection, diffusion, and migration resulting from the pressure difference, concentration gradient, and electric potential gradient, respectively [18,23]. Ions in the mobile region of the EDL are transported along with the flow through the channel length L, commonly inducing the electric convection current (i.e., streaming current) I_S for arbitrary cross section ($=\int_{\mathrm{Area}} \rho_e v_z dA$). The accumulation of ions sets up an electric field E_z with the streaming potential difference $\Delta\phi(=E_z L)$. Subsequently, this field causes the conduction current $I_C(=\Delta\phi/R_{\mathrm{Tot}})$ to flow back in the opposite direction. The total resistance $R_{\mathrm{Tot}} = (R_s^{-1} + R_f^{-1})^{-1}$consists of the surface resistance $R_s(=[R_{s,T}^{-1} + R_{s,B}^{-1} + R_{s,R}^{-1} + R_{s,L}^{-1}]^{-1})$ and the fluid resistance R_f in parallel, expressed as

$$R_s = \frac{L}{W(\lambda_{s,T} + \lambda_{s,B}) + H(\lambda_{s,R} + \lambda_{s,L})}, \tag{11}$$

$$R_f = \frac{L}{\int_0^H\int_0^W \lambda_f(x,y)\,dx\,dy}. \tag{12}$$

In Eqs. (11) and (12), the specific surface conductivity λ_s depends on the property of the channel wall and $\lambda_f(= \Lambda^2 e^2 N_A[K_+ n_+(x,y) + K_- n_-(x,y)])$ indicates the local fluid conductivity. Here, the mobility $K_i(= D_i/kT)$ is defined as the velocity of ion species i in the direction of an electric field of unit strength with diffusivity D_i for cations (+) and anions (−). At the steady state, the net current I consisting of I_S and I_C should be zero, viz., $I \equiv I_S + I_C = 0$. Following this relationship in generic form, one expects to derive $\Delta\phi(= -I_S R_{\mathrm{Tot}})$ as $-R_{\mathrm{Tot}}\int_0^H\int_0^W \rho_e(x,y)\,v_z(x,y)\,dx\,dy$.

C. Computations

The electric potential is first obtained by solving Eq. (4) based on the finite-difference method (FDM), of which basic procedures are analogous to the previous work [13,14]. The five-point central-difference method enables one to solve the finite-difference equation by successive under-relaxation iterative calculation. The fluid-velocity profile can be computed by solving the aforementioned N-S equation of Eqs. (6)–(8) together with charge conservation derived from N-P principle. The well-established SIMPLE algorithm represented by the finite-volume method (FVM) was employed to solve the unknown pressure terms $p(x,y)$ of the N-S equation by using the continuity equation ($\nabla \cdot \boldsymbol{v} = 0$) as the pressure-velocity coupling. Detailed discussion of the SIMPLE is available in the literature [22]. Accomplishing the velocity and pressure corrections, we repeat the sequence of operations until the convergence is guaranteed. The staggered grid and an ADI method are adopted when the procedure comes to treat x and y components of the discretized N-S equation and the continuity equation. In this, the staggered grid is half-node shifted from the original grid for the momentum equation, which prevents the failure of pressure estimations and assures calculations that are more accurate.

After the mesh refinement with a grid convergence test to yield satisfactory accuracy, the computational domain is discretized into 151×151 equally spaced grid points in both the x and y directions. Convergence criteria are specified with the relative variation between two successive iterations to be smaller than the preassigned accuracy level of 10^{-8}. The convergence is fast, and 250–300 iterations were enough to achieve convergence for the present channel dimension.

III. RESULTS AND DISCUSSION

Illustrative computations are performed considering the 1-1 type electrolyte of KCl fluid ($\rho = 10^3$ kg/m^3, $\mu = 10^{-3}$ Pa s) with applied pressure drop ($\Delta p/L$) of 1 bar/m. From the molar conductance of infinite dilution related to the ion migration [13], the individual mobilities of ions K_i in aqueous solutions at RT are evaluated as 7.91×10^{-13} and 8.19×10^{-13} mol s/kg for K^+ and Cl^-, respectively. The value of the fluid conductivity of KCl is applied from the previous study [13], and the specific surface conductivity of glass and PDMS is taken as 10^{-2} μS and 5×10^{-2} nS, respectively [23,24]. Reciprocal aspect ratios are chosen as $H/W = 0.25$ and 4.0 for the prototype of shallow (or low-aspect-ratio) and deep (or high-aspect-ratio) channels.

The electrokinetic strength originated from long-range electrostatic repulsion increases by either thickening the EDL or increasing the electric surface potential. We consider a strong electrokinetic interaction with extremely low ionic strength of 10^{-4} mM KCl electrolyte that is presumably similar to a state of the deionized and distilled water. It provides the greatest EDL thickness $\kappa^{-1} = 965$ nm. Under overlapped EDL conditions, the coupled Poisson and N-P equations can give more accurate potential and ionic distributions beyond the P-B equation [25]. However, $\kappa R_h > 3$ is valid for applying the P-B with acceptable accuracy. The magnitude of dimensionless surface potential $\Psi_s (= \psi_s e/kT)$ at medium pH 7 can be taken by the zeta potential data. According to a great deal of previous reports [26–28], the zeta potential for $10^{-1} \sim 10^{-4}$ mM 1-1 type electrolyte is found to vary from -25 to -100 mV for PDMS and from -50 to -200 mV for glass surfaces, depending on the electrolyte concentration and the condition of surface treatment.

A number of experimental studies have been conducted to determine the slip length β in pressure-driven flows, and it depends on the experimental conditions, such as solution environment, shear rate, and surface roughness [29–31]. Recent measurements performed in our group by particle streak velocimetry with an epi-fluorescence microscope reveal β in partially nonwetting PDMS surfaces (contact angle of about 98°) to be ranging from several hundreds of nanometers to 1 μm, for less than the critical shear rate. We need to pursue its accurate value, however, a more detailed discussion of this issue is beyond the scope of this study.

The electric potential profile moves toward a center region of the channel by repulsive screening (cf. increasing κ^{-1} by decreasing electrolyte concentration). Invoking the electroviscous effect, the velocity decreases in accordance with the increasing electrokinetic interaction that involves either higher Ψ_s or weaker screening with larger κ^{-1}. As recognized in the previous study [16], the numerical code has been validated by the fact that the velocity prediction matches the analytical problem of inert flows in a straight channel ($W/R_C \to 0$), although its figure is not presented here. Axial velocity profiles at the horizontal cut (i.e., $H/2$) along the streamwise direction maintain a fully developed state in the entire region of the curved channel except for the entrance. To ensure the axial independence of the velocity ($\partial v_z/\partial z = 0$), the velocity and pressure fields are analyzed in the transverse section (i.e., r and y directions) at the middle of the turn.

A. Spanwise and streamwise velocities with variations of channel dimension

Figure 3 shows the pressure and velocity fields in shallow and deep channels with dissimilar wall conditions of glass in the top and bottom and PDMS in the right and left sides, where $R_h = 3.2$ μm and $\kappa R_h = 3.3$. A qualitative difference in the contours of the spanwise pressure gradient directing to the inner wall from the outer wall can not be observed between two channels. This pressure distribution along the spanwise direction results from a gap of the flow path between the inner (arc AB) and the outer (arc $A'B'$) walls of a curved channel in Fig. 2. In Fig. 3, the maximum spanwise velocity is located along the central line of the shallow channel ($H/W = 0.25$), whereas it is certainly divided into above and below the plane of symmetry of the deep channel ($H/W = 4.0$). The magnitude of the spanwise velocity is smaller in the order of $10^{-5} \sim 10^{-7}$ than that of the axial velocity, verifying again the aforementioned assumption of purely streamwise dependence of the flow-induced electric field.

The Reynolds number ($\mathrm{Re} = 2R_h\rho\langle v_z\rangle/\mu$) and nondimensional curvature are combined into the Dean number ($\mathrm{De} = \mathrm{Re}\sqrt{W/R_C}$) that has physical significance quantifying the inertial force in curved channels. The De for the conditions in Fig. 3 is estimated at very low values in the order of $10^{-3} \sim 10^{-4}$. Accordingly, a dominant effect of the spanwise

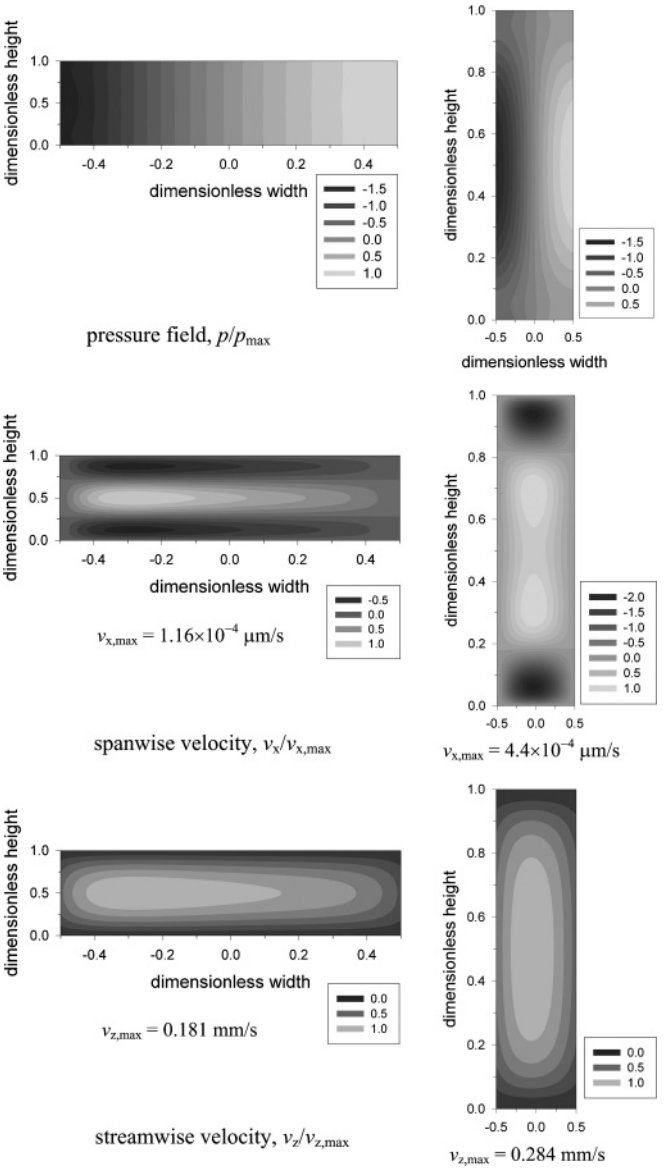

FIG. 3. The contour plots of pressure field, spanwise velocity, and streamwise velocity for shallow (lying figure: $H = 4$ μm, $W = 16$ μm) and deep (standing figure: $H = 16$ μm, $W = 4$ μm) channels with glass in the top and bottom and PDMS in the right and left sides, where $W/R_C = 0.5$, $\Delta p/L = 1$ bar/m, $\kappa^{-1} = 965$ nm, $\psi_{s,\mathrm{PDMS}} = -60$ mV, $\psi_{s,\mathrm{glass}} = -120$ mV, and numbers in the legend are normalized by a maximum value.

pressure gradient over the fluid inertia by centrifugal force permits the streamwise axial velocity to shift toward the inner region of the channel, as reported in the literature [16,32,33]. If the inertial force plays an evident role as the De gets higher enough, the axial velocity profile becomes skewed into the

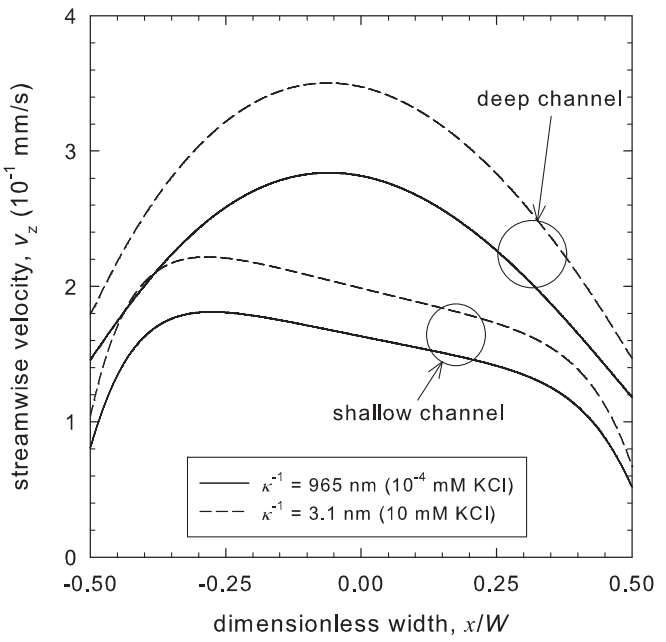

FIG. 4. The streamwise velocity profiles at the position of $H/2$ for glass-PDMS shallow and deep channels with different EDL thickness, where conditions are the same as in Fig. 3.

outer wall as observed in the channels with R_h above the millimeter scale. Compared to the case of the deep channel, the portion of the maximum axial velocity in the shallow channel (lower H/W) is clearly forced to the inner wall, resulting from the fact that the greater distance traveled by the fluid along the outer wall further broadens the profile.

In order to interpret the contribution of electrokinetic effect due to the EDL thickness, the streamwise velocity profiles at $H/2$ of very low ionic concentration are compared to those of exemplary concentration (i.e., 10 mM electrolyte) normally found in the real LOCs. In Fig. 4, the velocity increases in accordance with the decreasing electrokinetic interaction by stronger screening with smaller EDL thickness. The extent of increasing streamwise velocity is estimated as, on average, 22% for the deep and 21% for the shallow channel. The velocity enhancement by the fluid slip is stronger in the deep channel than in the shallow one, because the PDMS surface in the deep channel occupies a larger area of right and left sides.

Further computations were performed for a wide range of channel cross-sectional dimension of $R_h = 3.2$ μm (4×16, 16×4 μm^2), 6.4 μm (8×32, 32×8 μm^2), 12.8 μm (16×64, 64×16 μm^2), and 25.6 μm (32×128, 128×32 μm^2) to verify the trend of accompanying changes in spanwise and streamwise velocities. As tabulated in Table I, the De number increases in response to an increase of R_h, implying the contribution of fluid inertia. From Fig. 5, it is emphasized

TABLE I. List of dimensionless parameters and their ranges applied in this paper.

Dimensionless parameter	H/W	W/R_C	Re, De			
			$\kappa R_h = 3.3$	$\kappa R_h = 6.6$	$\kappa R_h = 13.3$	$\kappa R_h = 26.5$
Value	$0.25 \sim 4.0$	$0.1 \sim 1.0$	$10^{-3} \sim 10^{-4}$	$O(10^{-3})$	$O(10^{-2})$	$O(10^{-1})$

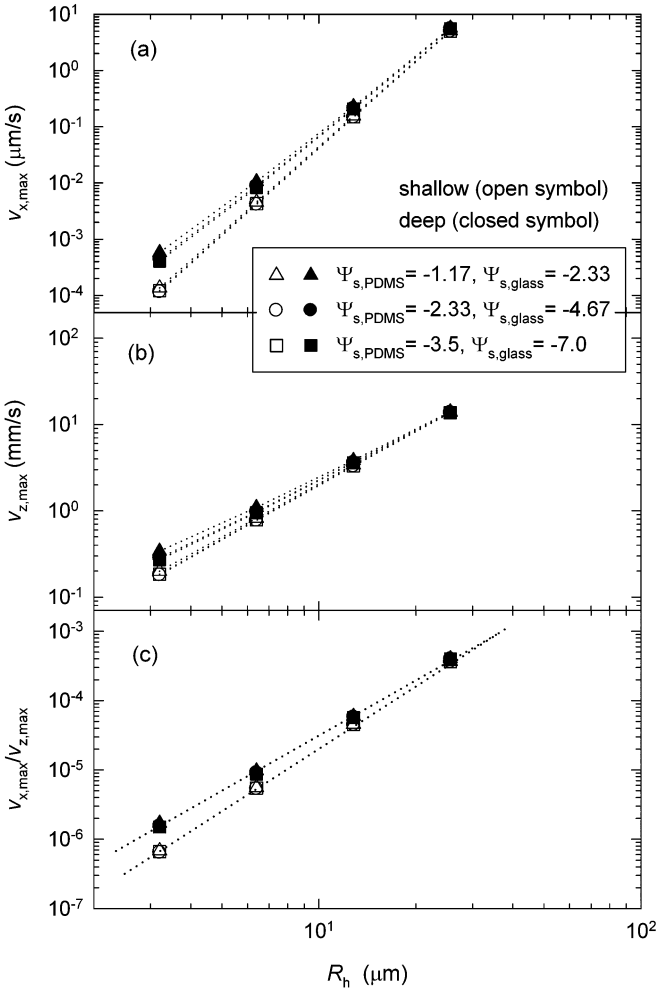

FIG. 5. Dependence on the hydraulic radius R_h of glass-PDMS shallow and deep channels at $\kappa^{-1} = 965$ nm: (a) $v_{x,\max}$, (b) $v_{z,\max}$, and (c) $v_{x,\max}/v_{z,\max}$, where other conditions are the same as in Fig. 3.

that the magnitude of spanwise and streamwise velocities as well as their ratio increase with increasing dimension of the channel cross section. For $R_h = 25.6$ μm (cf. 32×128 or 128×32 μm^2) with the same pressure gradient, the spanwise and streamwise velocities have the orders of several μm/s and cm/s, respectively, in which their ratio becomes an order of 10^{-4}. While the dependence of surface potential is very weak in the shallow channel, a higher dependency is found in the smaller R_h regime of the deep channel, pertaining to the electroviscous effect. The log-log plots of Fig. 5 provide a result of scaling relations as $\sim R_h^{\alpha}$ with the slope α. The exponent ($=\alpha$) for $v_{x,\max/v_z,\max}$ is obtained as about 3 and 2.8 for shallow and deep channels, respectively, without the surface potential dependency. The linear relationship can also be found in the log-log plot with respect to the De or Re number.

B. The secondary-flow motion in the dissimilar channel wall

We make three kinds of configurations with setting four sides of channel walls as (case I) purely glass, (case II) glass in the top and bottom and PDMS in the right and left sides (cf. previous section), and (case III) glass in the bottom and PDMS in the other sides. Uniform surface properties in case I result from the dry etching of the glass channel plate and then anodic bonding with glass coverslip. Applying the sandwich molding process results in case II, where the glass plate becomes the top and bottom surfaces, but both sidewalls are built by PDMS. Bonding the molded PDMS channel prepared by soft lithography and the glass coverslip creates the wall configuration of case III, as in Fig. 1.

Holding the axial independence of the streamwise velocity, the vorticity profiles are also obtained at the middle of the turn. The smaller dimension of the channel cross section has the advantage of allowing independent streamwise vorticity evolution. In any cases, streamline results reveal that curvature introduces a secondary rotational flow-field perpendicular to the flow direction (namely Dean flow) with the upper anticlockwise and the lower clockwise. Figures 6 and 7 provide the vortices results in shallow and deep channels, respectively, where β at the hydrophobic PDMS surface is held a higher value of 1 μm (cf. $\kappa\beta \cong 1$) and the magnitude of difference between each contour line is equal. A pair of counter-rotating vortices placed above and below the plane of symmetry of the channel is common in cases I and II of the shallow channel, as shown in Fig. 6. Compared to these, the contour of case III shows a different shape, in which the vortex nearby

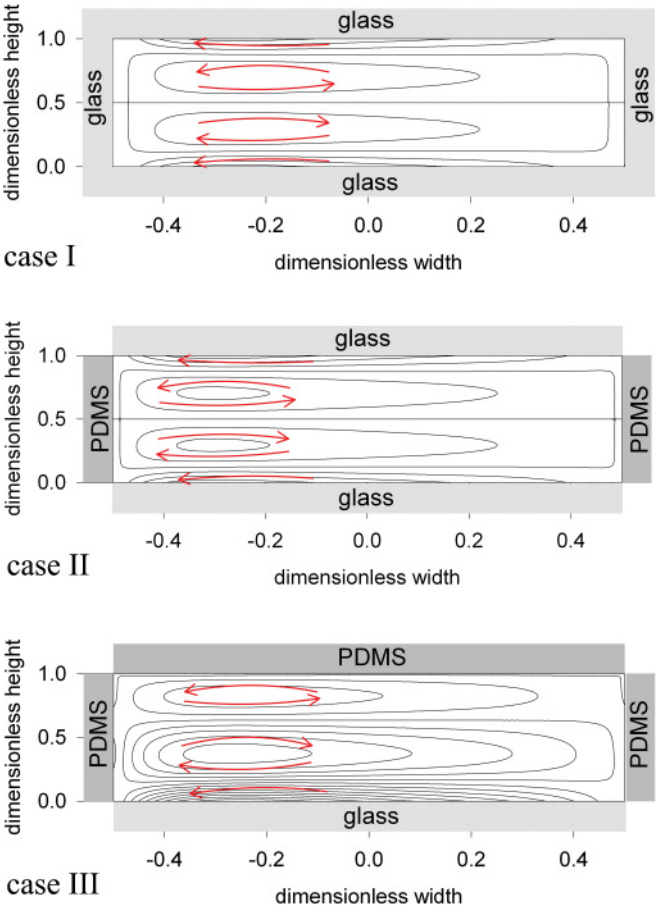

FIG. 6. (Color online) The contour plots of vorticity in a rectangular cross section of the shallow channel for different surface heterogeneity with glass and PDMS, where conditions are same as in Fig. 3.

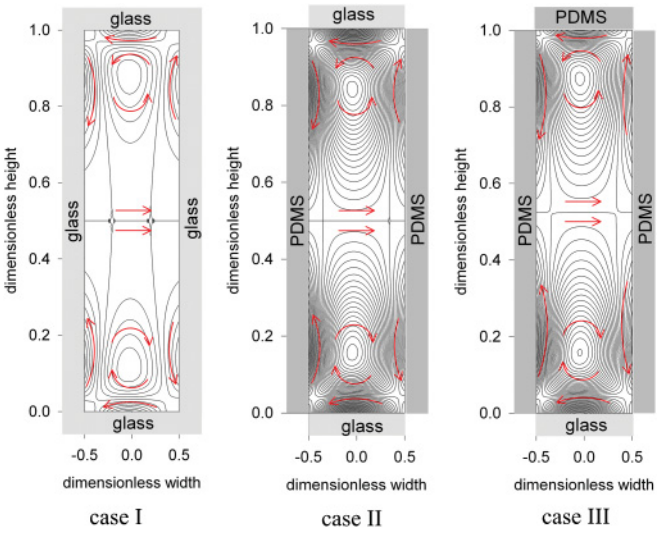

FIG. 7. (Color online) The contour plots of vorticity in a rectangular cross section of the deep channel for different surface heterogeneity with glass and PDMS, where conditions are the same as in Fig. 3.

glass wall is developed largely and strongly. As a result, the size of the vortex cell is asymmetric and the location of two counter-rotating vortices moves above the symmetric plane of the channel. This behavior can be checked consistently on the contour of the streamline that spreads on the other side. In Fig. 7, both the shape and the close pattern of the vorticity profile are almost the same between cases II and III. On the contrary, it is obvious that the vorticity profile of case I demonstrates the loose-distribution pattern, especially in the vicinity of mid-plane. Another feature can be seen, i.e., the positions of a pair of maximum vortices approach closer to the top and bottom surfaces.

By noting that the axial velocity profile becomes skewed into the inner wall, we need to determine the shifting of the spanwise position (x/W) of maximum axial velocity according to variations of the curvature radii R_C for constant W. In Fig. 8, the degree of shift toward the inner wall increases with an increase of the curvature ratio W/R_C, leading to a rapid turn. When $W/R_C = 1.0$, its magnitude in the shallow channel is higher by about 2.2–3.7 times, compared to the deep channel. The attributed reason for this feature was already discussed in Fig. 3. In both the shallow and deep channels, the purely glass channel reveals lesser shifting than heterogeneous configurations of the channel wall. In the shallow channel, the axial velocity of case II tends to shift toward the inner wall much more than that of case III. Unlike the case of the shallow channel, no difference exists between cases II and III in the deep channel, indicating that the wall condition of the top and bottom surfaces does not affect the degree of shift in the deep channels. Therefore, it is evident that both the axial velocity and vorticity profiles depend on the surface heterogeneity of the channel wall taking a large area.

C. The fluid-slip effect

The effect of the strength of fluid slip was checked by obtaining both the axial velocity and vorticity profiles with

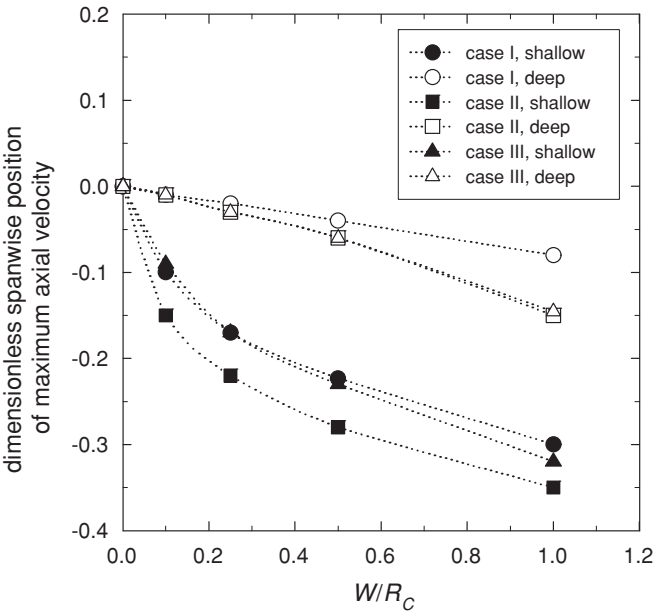

FIG. 8. The evolution of nondimensional spanwise position of maximum axial velocity with variations of curvature ratio in shallow and deep channels for different surface heterogeneity with glass and PDMS.

variations of slip length β widely ranging up to 1 μm (i.e., $\beta/R_h = 0.3125$). For illustrations, four sides of the channel wall with the uniformly hydrophobic PDMS surface are considered, for conditions that are otherwise the same as in Fig. 3. Figure 9 shows that the electrokinetic effect in the deep channel with $W/R_C = 0.1$ does not contribute to the spanwise shifting of maximum axial velocity. In the other cases, it causes the change in the spanwise shifting with the relative difference ranging from 6 to 33%. This spanwise shifting is

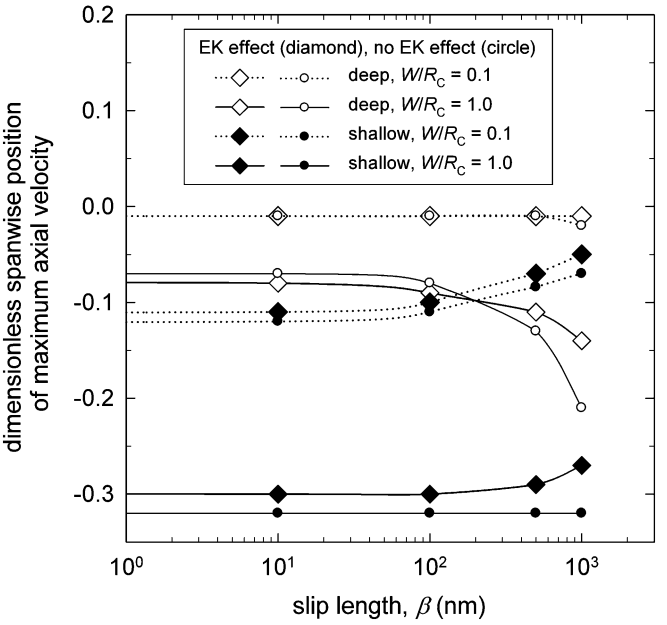

FIG. 9. The evolution of nondimensional spanwise position of maximum axial velocity with variations of β in hydrophobic shallow and deep channels for different curvature ratios.

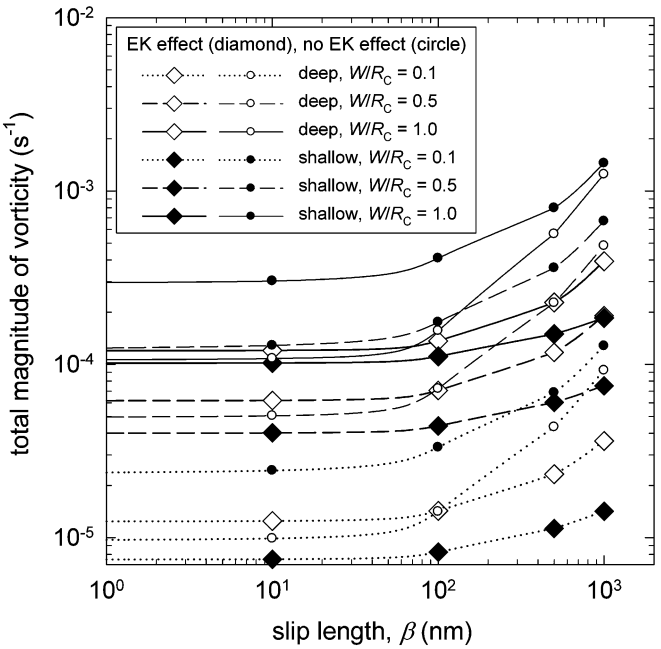

FIG. 10. The evolution of total magnitude of vorticity with variations of β in hydrophobic shallow and deep channels for different curvature ratios.

almost independent of variations of the slip length for the deep channel in $W/R_C = 0.1$ and the shallow channel without electrokinetic effect in $W/R_C = 1.0$, but the other cases show the dependency for $\beta > 100$ nm. As β increases, the behavior of shift toward the inner wall becomes stronger in the deep channel, while it becomes lesser in the shallow channel.

Estimating the total magnitude of vorticity $\sum |\omega_z|$ at the specified cross section of the channel allows us to predict the circulation strength in the secondary flow. Such a flow motion provides a useful tool in the microfluidic mixing system and the manipulation of particles or cells [34]. In Fig. 10, $\sum |\omega_z|$ increases with increasing channel curvature W/R_C, evidencing again the contribution of fluid inertia. One can find the presence of the distinguishable contribution of electrokinetic effect in the magnitude of vorticity. With the electrokinetic effect, the deep channel represents higher $\sum |\omega_z|$ than the shallow channel for the same conditions. This trend is related to the fact that the deep channel takes the close pattern in the vorticity profile. The magnitude of vorticity involving electrokinetic effect does not depend on the fluid slip for β less than about 50 nm. It is noteworthy that, for $\beta > 50$ nm, $\sum |\omega_z|$ increases with increasing fluid slip, being explained by the contribution of enhanced axial velocity driven by the slip. As obtained so far, the numerical framework established in this paper has an impact on applications to the situation in which the channel may be made of any walls of either no-slip or slip conditions with different geometry, once their properties are provided.

IV. CONCLUSIONS

Our recent research has been extended to an analysis of the secondary Dean flow behavior in shallow and deep channels under dissimilar wall conditions of the charged and slip properties. The pressure-driven electrokinetic flow in curved rectangular microchannels was explored by establishing theoretical models with relevant coupled equations and numerical framework. The electrokinetic body force originated from the nonlinear P-B field for strongly interacting EDLs and the flow-induced electric field was implemented in the N-S equation associated with the charge conservation. A generalized slip BC, exactly derived for curved surfaces, was applied at the hydrophobic channel wall.

For very low Dean numbers found in this study, the effect of spanwise pressure gradient would be an overwhelming emphasis on the inertial force, from which an inward skewness was observed in the axial velocity profile with a secondary motion relevant to the microfluidic mixing. The magnitude of spanwise velocity increases abruptly with increasing channel cross-sectional dimension, which was predicted by scaling with the exponent. Three kinds of different wall conditions were considered with negatively charged glass and PDMS for both cases of shallow and deep microchannels. It should be noted that the skewed velocity and vorticity patterns are influenced by the channel aspect ratio and surface heterogeneity, in addition to the channel curvature W/R_C and the De value. In the region of higher fluid slip ($\beta/R_h > 0.031$), as the slip length β increases, the shifting of the axial velocity toward the inner wall varies and the circulation strength in the secondary flow increases due to the enhanced axial velocity.

ACKNOWLEDGMENTS

This research was supported by the Basic Research Fund (No. 20100021979) and the Converging Research Center Program (No. 2009-0082136) through the National Research Foundation of Korea. The author thanks J.-M. Lim for his assistance.

[1] W.-H. Tan and S. Takeuchi, Proc. Natl. Acad. Sci. USA **104**, 1146 (2007).
[2] B. Paegel, L. Hutt, P. Simpson, and R. Mathies, Anal. Chem. (Washington, DC, US) **72**, 3030 (2000).
[3] H. Chen and J. C. Meiners, Appl. Phys. Lett. **84**, 2193 (2004).
[4] C. T. Culbertson, S. C. Jacobson, and J. M. Ramsey, Anal. Chem. (Washington, DC, US) **70**, 3781 (1998).
[5] H. A. Stone, A. D. Stroock, and A. Ajdari, Annu. Rev. Fluid Mech. **36**, 381 (2004).
[6] T. M. Squires and S. R. Quake, Rev. Mod. Phys. **77**, 977 (2005).
[7] M. Napoli, J. C. T. Eijkel, and S. Pennathur, Lab Chip **10**, 957 (2010).
[8] C.-L. Rice and R. Whitehead, J. Phys. Chem. **69**, 4017 (1965).
[9] S. Levine, J. R. Marriott, G. Neale, and N. Epstein, J. Colloid Interface Sci. **52**, 136 (1975).
[10] C. Yang and D. Li, J. Colloid Interface Sci. **194**, 95 (1997).
[11] L. Hu, J. D. Harrison, and J. H. Masliyah, J. Colloid Interface Sci. **215**, 300 (1999).
[12] J. Yang and D. Y. Kwok, Langmuir **19**, 1047 (2003).

[13] M.-S. Chun, T. S. Lee, and N. W. Choi, J. Micromech. Microeng. **15**, 710 (2005).
[14] M.-S. Chun, T. S. Lee, and K. Lee, Korea-Australia Rheol. J. **17**, 207 (2005).
[15] L. Gong, J. Wu, L. Wang, and K. Cao, Phys. Fluids **20**, 063603 (2008).
[16] J. H. Yun, M.-S. Chun, and H. W. Jung, Phys. Fluids **22**, 052004 (2010).
[17] B.-H. Jo, L. M. Van Lerberghe, K. M. Motsegood, and D. J. Beebe, J. Microelectromech. Syst. **9**, 76 (2000).
[18] J. H. Masliyah and S. Bhattacharjee, *Electrokinetic and Colloid Transport Phenomena* (Wiley, Hoboken, 2006).
[19] C. L. M. H. Navier, Mem. Acad. Sci. Inst. France **6**, 389 (1823).
[20] E. Lauga and H. A. Stone, J. Fluid Mech. **489**, 55 (2003).
[21] L. Bocquet and J.-L. Barrat, Soft Matter **3**, 685 (2007).
[22] S. V. Patankar, *Numerical Heat Transfer and Fluid Flow* (McGraw-Hill, New York, 1980).
[23] C. Werner, H. Körber, R. Zimmermann, S. Dukhin, and H.-J. Jacobasch, J. Colloid Interface Sci. **208**, 329 (1998).
[24] Z. A. Almutairi, T. Glawdel, C. L. Ren, and D. A. Johnson, Microfluid. Nanofluid. **6**, 241 (2009).
[25] W. Qu and D. Li, J. Colloid Interface Sci. **224**, 397 (2000).
[26] M. Mala, D. Li, C. Werner, H.-J. Jacobasch, and Y. B. Ning, Int. J. Heat Fluid Flow **18**, 489 (1997).
[27] B. J. Kirby and E. F. Hasselbrink Jr., Electrophoresis **25**, 203 (2004).
[28] J. Song, J. F. L. Duval, M. A. C. Stuart, H. Hillborg, U. Gunst, H. F. Arlinghaus, and G. J. Vancso, Langmuir **23**, 5430 (2007).
[29] D. C. Tretheway and C. D. Meinhart, Phys. Fluids **14**, L9 (2002).
[30] P. Joseph and P. Tabeling, Phys. Rev. E **71**, 035303R (2005).
[31] P. Huang, J. S. Guasto, and K. S. Breuer, J. Fluid Mech. **566**, 447 (2006).
[32] B. Snyder and C. Lovely, Phys. Fluids A **2**, 1808 (1990).
[33] Y. Yamaguchi, F. Takagi, K. Yamashita, H. Nakamura, H. Maeda, K. Sotowa, K. Kusakabe, Y. Yamasaki, and S. Morooka, AIChE J. **50**, 1530 (2004).
[34] H. Song, Z. Cai, H. Noh, and D. J. Bennett, Lab Chip **10**, 734 (2010).